Visualization of the Cellulose Biosynthesis and Cell Integration into Cellulose Scaffolds

5 AUTHORS, INCLUDING:

Christian Brackmann
Lund University
57 PUBLICATIONS **773** CITATIONS

Annika Enejder
Chalmers University of Technology
55 PUBLICATIONS **1,361** CITATIONS

Visualization of the Cellulose Biosynthesis and Cell Integration into Cellulose Scaffolds

Christian Brackmann,[†] Aase Bodin,[‡] Madeleine Åkeson,[†] Paul Gatenholm,[‡] and Annika Enejder*,[†]

Molecular Microscopy and Biotechnology/Biopolymer Technology, Department of Chemical and Biological Engineering, Chalmers University of Technology, Kemivägen 10, S-412 96 Göteborg, Sweden

By controlling the microarchitecture of bioengineered scaffolds for artificial tissues, their material and cell-interaction properties can be designed to mimic native correspondents. Current understanding of this relationship is sparse and based on microscopy requiring harsh sample preparation and labeling, leaving it open to which extent the natural morphology is studied. This work introduces multimodal nonlinear microscopy for label-free imaging of tissue scaffolds, exemplified by bacterial cellulose. Unique three-dimensional images visualizing the formation of nanofiber networks throughout the biosynthesis, revealing that supra-structures (layered structures, cavities) are formed. Cell integration in compact scaffolds was visualized and compared with porous scaffolds. While the former showed distinct boundaries to the native tissue, gradual cell integration was observed for the porous material. Thus, the degree of cell integration can be controlled through scaffold supra-structures. This illustrates the potential of nonlinear microscopy for noninvasive imaging of the intriguing interaction mechanisms between scaffolds and cells.

1. Introduction

The development of replacement tissues to lost structures, or even whole organs, largely relies on natural materials of different structural and functional properties. Artificial extracellular tissue scaffolds can be constructed from natural components extracted from mammalian tissues,[1] from fibril networks engineered from biopolymers,[2,3] from cellulose constructs woven by bacteria[4] at different morphologies,[5] and from genetically encoded polypeptides.[6] Their biological, physical, and mechanical properties can be further fine-tuned by forming composites of natural fibers on one hand and ceramic materials,[7] carbon nanotubes,[8] biocompatible synthetic polymers,[9,10] or electrospun nanofibers[11] on the other. It is crucial to produce artificial tissue scaffolds with an appropriate morphology and biological environment, promoting cell in-growth, differentiation, and eventually deposition of extracellular matrix components. This can be achieved either by natural regeneration of cells in situ in the host organ or by preseeding the artificial scaffolds with cultured, autologous cells or stem cells for appropriate differentiation.[12] Thus, advanced protocols to produce artificial tissues already exist, and advances in bio- and nanotechnology, proteomics, and stem cell biology promote future scaffolds with targeted cell interaction. This demands methods able to characterize the morphology of *intact* constructs at macromolecular level in three-dimensions and to monitor their interaction with the host tissue in vivo.

Unfortunately, conventional technology has difficulties meeting up with all these requirements. Electron microscopy is a well-established, high-resolution (∼10 nm) technique for characterization of morphology. However, the extensive sample preparation involves fixation, dehydration, freeze-drying, and material coating,[13,14] all potentially affecting the material properties and excluding the observation of a scaffold-cell system under native conditions. In addition, only the most superficial material region is probed, requiring physical sectioning to access the scaffold interior, which in turn could introduce compression artifacts in the architecture. Atomic force microscopy (AFM) also permits surface characterization at a highly detailed level; however, the tendency of the probe tip to stick to a soft material is a serious limitation for investigations of tissue.[15]

Confocal fluorescence microscopy offers access to the scaffold interior via optical sectioning at a spatial resolution of ∼1 μm.[16] However, usually a fluorescent marker that attaches to the structure or cellular component of interest is required, which introduces uncertainties related to the uptake and expression of the fluorophore. Furthermore, photobleaching effects prevent long-term studies of cell−scaffold interaction processes and the labeling often affects the viability of living matter; for example, efforts to study the morphology of bacterial cellulose scaffolds have shown that labeling inhibits the formation of the nanofibrils.[17] Altogether, restrictions associated with conventional characterization technologies limit understanding of the relationship between structural and functional properties of the advanced constructs presently appearing within tissue engineering. Nondestructive, label-free techniques are required for three-dimensional monitoring of the formation processes and final architecture of artificial extracellular matrices as wells as of cell integration and interaction processes in vivo.

Laser-based nonlinear microscopy techniques such as second harmonic generation (SHG) and coherent anti-Stokes Raman scattering (CARS) probe intrinsic optical material properties and allow for label-free imaging with high spatial resolution in three dimensions. SHG visualizes noncentrosymmetric ordered structures, demonstrated both for native[18–20] and artificial tissues.[21,22] In CARS microscopy interaction with molecular vibrational resonances makes selective, label-free imaging possible,[23,24] in particular of lipid distributions due to efficient signal generation

* Corresponding author. Phone: + 46 31 772 3852. Fax: + 46 31 772 3801. E-mail: enejder@chalmers.se.
† Molecular Microscopy and Biotechnology.
‡ Biopolymer Technology.
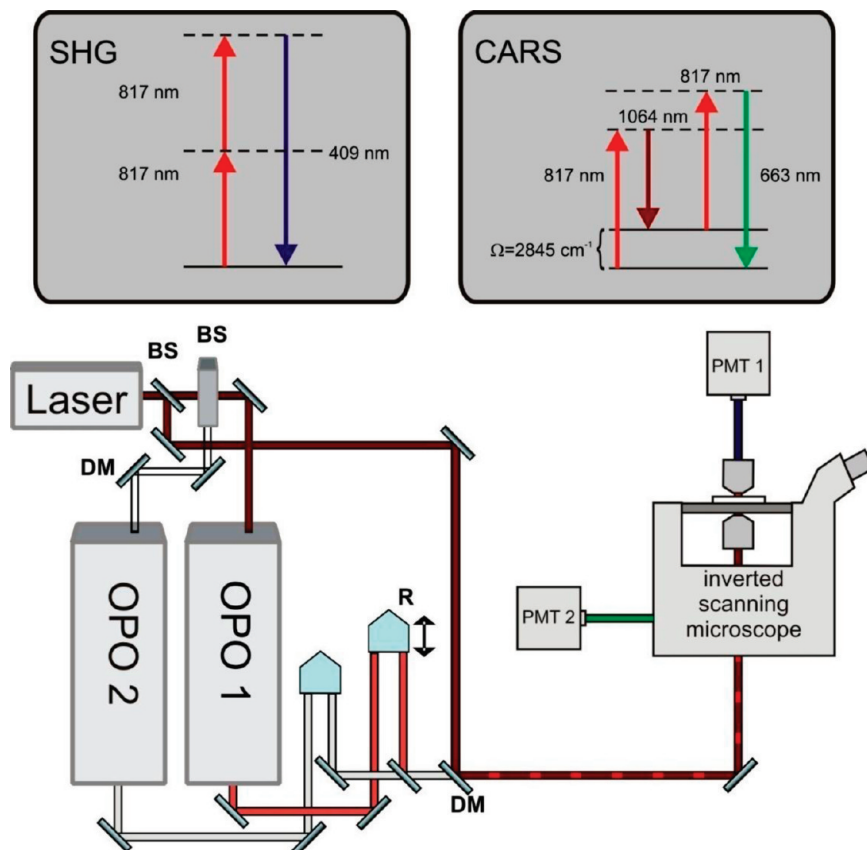
Figure 1. Outline of the experimental setup for multimodal nonlinear microscopy, showing the pulsed laser system consisting of a Nd:Van laser and two optical parametric oscillators (OPOs), the inverted scanning microscope, and the dual-channel detection system. Abbreviations: BS, beam splitter; DM, dichroic mirror; R, retro-reflector; PMT, photomultiplier tube. The insets show the excitation schemes for the techniques second harmonic generation (SHG) and coherent anti-Stokes Raman scattering (CARS) as simplified energy level diagrams.

in lipid acyl chains. Combined methods in multimodal nonlinear microscopy enable colocalization studies of interaction between tissue components and cells, which has been carried out on arterial cells,[25] cardiovascular structures,[26] and scaffolds of engineered tissue.[27] In addition, an overview of spectroscopy and imaging techniques for studies of engineered tissues has been presented by Georgakoudi et al.[28]

In this study, the build-up process of bacterial cellulose scaffolds is followed on a single bacterium/fiber level by colocalizing simultaneously collected CARS and SHG images of living, cellulose-weaving *Acetobacter xylinum* and produced cellulose fibers, respectively. The ability of multimodal nonlinear microscopy to provide valuable insights in tissue engineering is further demonstrated with CARS-SHG overlay images of implanted bacterial cellulose scaffolds. Scaffolds with different supra-structures showed differences in the degree of integration of adipocytes and extracellular matrix components from the host tissue, pointing out a relationship between the microarchitecture and biological function of artificial tissue constructs.

2. Experimental Section

2.1. Preparation of Tissue Scaffolds. The strain *Acetobacter xylinum* subsp. sucrofermentas BPR2001, tradenumber 1700178TM, was purchased from the American Type Culture Collection and cultures were maintained on complex media, as previously described.[29] Four colonies, grown on agar plates for 5−7 days at 30 °C, were transferred to a flask containing 100 mL of culture medium and 75 μL of filtered Celluclast (Novo Enzymes) and cultured at 30 °C on a rotary shaker set at 120 rpm for 48 h. The suspension was then centrifuged at 10000 × g for 10 min[30] and the pellets were resuspended in a buffer of 50

mM NaH_2PO_4. The procedure was repeated three times after which 100 μL of the final cell suspension was inoculated into 900 μL of sterile media used for the single-fiber visualization studies (Figure 2a−d). For production of tubular geometries, the fermentation was carried out in the presence of permeable silicone tubes (Ø 4 mm, SMI) for oxygenation, as described in detail elsewhere.[5] The porous cellulose scaffold was prepared by use of tightly packed paraffin particles, in the size range of 300−500 μm, around the silicone support during the fermentation.[31] The cellulose was harvested after 7 days and purified by repetitive addition of sodium hydroxide with ethanol and tenside for removal of the paraffin, which was verified by infrared spectroscopy.

2.2. Implantation of Tissue Scaffolds. In a separate study to assess the biocompatibility of the material, scaffolds of compact and porous bacterial cellulose were implanted in female Wistar rats having initial weights of approximately 200−240 g. A 1 cm long incision was made on the back of the rats and four separate subcutaneous pockets were prepared, two on each side of the incision line and approximately 4 cm apart. The implants were inserted into the pockets without fixation and the samples were explanted for characterization after 10 weeks. The animal experiments were approved by the ethics committee at the University of Gothenburg and further details are presented by Helenius et al.[32]

2.3. Nonlinear Microscopy. An outline of the setup for multimodal nonlinear microscopy is shown in Figure 1. The main components are a laser system, consisting of a pulsed Nd:Van laser (Picotrain, HighQ Lasers GmbH), two optical parametric oscillators (Levante OPO, APE GmbH), and an inverted microscope (Eclipse TE-2000-E, Nikon). The Nd:Van laser emits pulses with a wavelength of 1064 nm, a duration of 7 ps, and a repetition frequency of 76 MHz. The average output power of the laser is 10 W, which is separated into three beams; two for pumping the OPOs and one directly guided into the microscope.

The OPOs in turn generate beams of individually tunable wavelengths in the two intervals 785−845 nm and 855−920 nm. The output beams of the OPOs and the 1064 beam are spatially overlapped and directed into the mirror scanning unit of the microscope. Prior to entering the scanner, the beam diameters are adjusted with a telescope. Temporal overlap between the laser pulses at the sample is achieved by delay lines with adjustable retro-reflectors for the OPO beams. The beams are focused on the sample by the objective (Nikon Plan Fluor 40× N.A. 1.3 or Nikon TIRF 100× N.A. 1.49 oil immersion objectives), which can be translated to obtain three-dimensional imaging by scanning horizontal planes at different vertical positions.

The detection system consists of two single-photon counting photomultiplier tubes (PMC 100-1 and PMC 100-20, Hamamatsu) that can be mounted for detection both in the forward direction of the laser beams (PMT 1 in Figure 1) and in the backward epi-direction (PMT 2 in Figure 1). The signal is collected using an aspherical lens (N.A. 0.8) in forward detection and by the objective complemented by a spherical lens ($f = +50$ mm) in epi-detection. In the case of dual-forward or dual-epi detection the two signals are separated by a dichroic beam splitter. The detection arrangement used depended on the particular experimental conditions and is described below.

The setup permits simultaneous second harmonic generation (SHG) and coherent anti-Stokes Raman scattering (CARS) microscopy and combined measurements were carried out using excitation with an 817 nm beam and the 1064 nm beam according to the schemes shown in the inserts of Figure 1. The SHG signal induced by the 817 nm beam was detected at 409 nm and the CARS signal generated by the combined beams, probing the molecular vibration of 2845 cm^{-1}, was detected at 663 nm. Bandpass filters were used to isolate the signals spectrally. Typical excitation powers at the sample were 100 mW for the 817 nm beam and 80 mW for the 1064 nm beam.

2.4. Microscopy Measurements and Sample Preparation. Time-lapse measurements of the cellulose fiber formation were carried out by simultaneously collecting images of forward-detected SHG signal and epi-detected CARS signal. The sample consisted of a silicone spacer attached to a microscope cover slide forming a chamber in which 10 μL of bacterial suspension was added. The chamber was partially covered with a second cover slide to delay drying while still permitting ambient oxygen to access the suspension, forming a viable environment for the bacteria.

The development of the bacterial cellulose network was followed in measurements carried out on cellulose tubes sampled from fermentors after a few hours, 1, 2, and 7 days, thus, covering the full seven-day growth process. The tubular samples were mounted between two cover slides using a spacer and the density of the material required collection of both signals in the epi-direction. Two- and three-dimensional images at an approximate depth of 10−50 μm were collected. A full radial scan (0−700 μm) of the distribution of bacteria and the fiber morphology throughout a seven-day sample was collected by 38 images, each 25 × 25 μm in size. The explanted compact and porous scaffold samples with integrated native cells were monitored by combined epi-detected SHG and CARS microscopy images, covering a field-of-view of 150 × 150 μm.

3. Results and Discussion

3.1. Visualization of the Build-Up Process of Bacterial Cellulose. In the time series of combined SHG and CARS microscopy images (Figure 2a−c), simultaneously measured on a culture of *Acetobacter xylinum*, the emergence of the initial cellulose nanofibrils can be followed. The molecular structure of the cellulose fibrils allows them to be visualized in the SHG images (blue color) overlaid with the corresponding CARS microscopy images of bacteria, generating a resonant signal from primarily lipid-rich cellular structures when probing the CH$_2$ vibration at 2845 cm^{-1}. Thus, the bacteria, rod-shaped objects color-coded in red, can be colocalized with the emerging
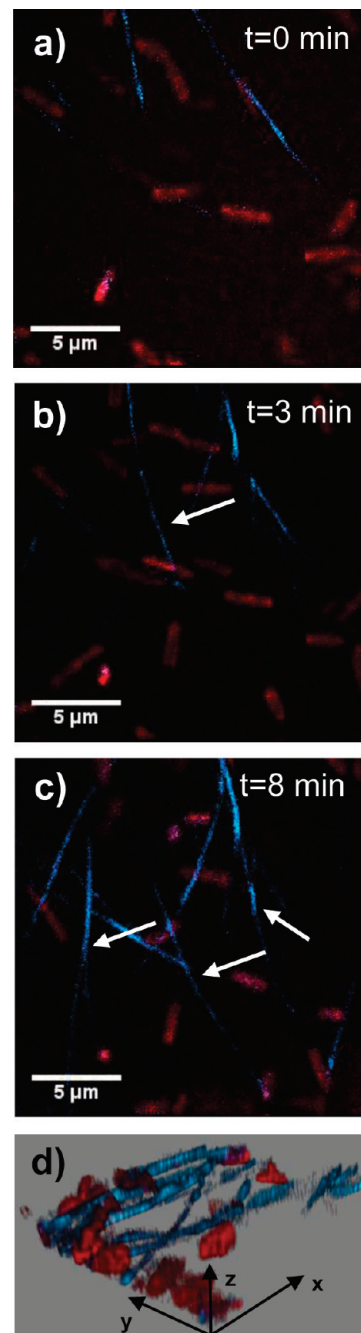
Figure 2. Overlay SHG (blue) and CARS (red) microscopy images measured during cellulose production in a bacterial suspension. Cellulose fibers are visualized by SHG and the hydrocarbon contents of the bacteria (red rod-shaped objects) are probed by CARS. Image size 20 × 20 μm, integration time 20 s. (a) Image measured immediately after sample preparation, (b) post 3 min, and (c) post 8 min. The arrow in (b) indicates an emerging fiber, shown to its full length 5 min later in (c). During these 5 min, new fibers also appear, such as the branched fiber arrangements indicated by additional arrows in (c). This confirms the viability of the bacteria in the microscopy cultivation chamber. (d) Three-dimensional representation showing a network of distinguishable fibers together with bacteria following approximately 10 min of growth. Note that the bacteria tend to align along the existing fibers.

nanofibrils. Initially, the bacteria are highly active, exhibiting Brownian-like motion close to the liquid/air interface at a speed of typically 1 μm/sec. Individual cellulose fibrils gradually start to appear, indicated by arrows in Figures 2a−c, over a time period of minutes. They are distributed over a few micrometers in depth, as shown in the three-dimensional volume image in
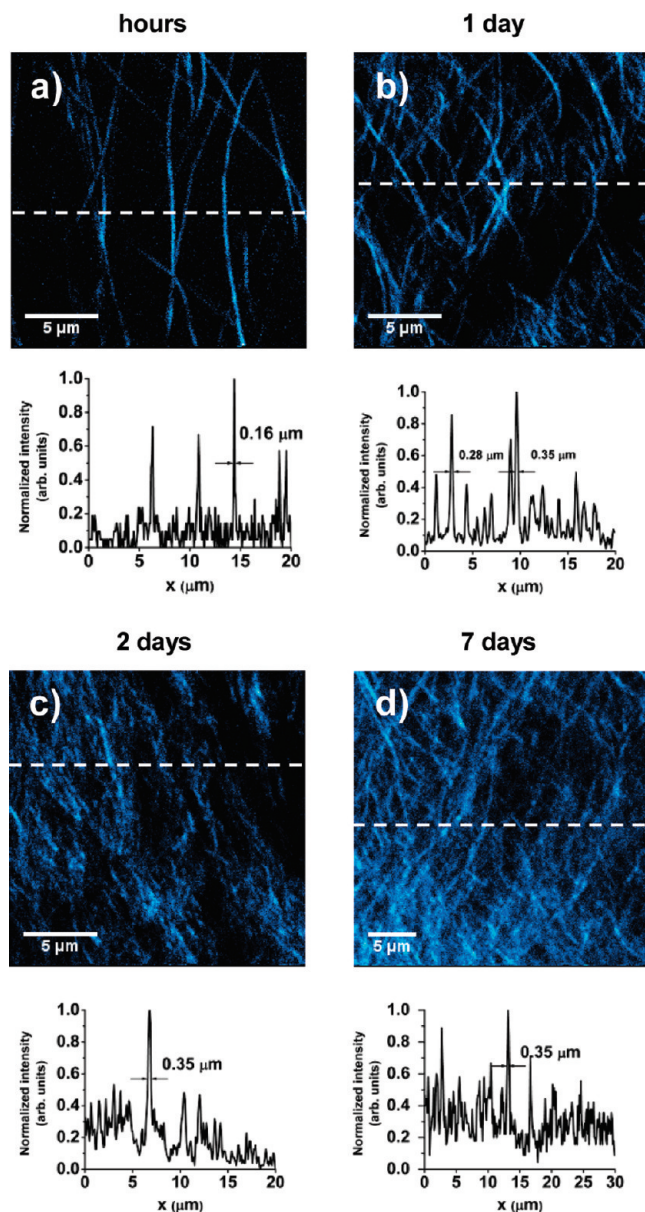
Figure 3. SHG microscopy images measured on bacterial cellulose tubes during the 7 day production period: (a) after a few hours of growth, (b) after 1 day, (c) after 2 days, and (d) after 7 days. Image sizes 20 × 20 μm (a–c) and 30 × 30 μm (d), integration times 20–300 s. The graphs show intensity profiles measured along the dashed lines in the images. High-intensity peaks represent fibers and diameters of isolated fibers can be estimated to ~200 nm. As cellulose density increases with time, observed as an increase in intensity profile background level, individual fibers become less distinguishable.

Figure 2d, visualizing slowly, translationally moving bacteria being restricted by the emerging cellulose matrix. The network of entangled fibers initially shows random character, though with a tendency toward an increasing degree of directionality and fiber alignment in the end-product matrix, which also has been observed by electron microscopy at stationary growth conditions.[14] This supports the approach to control material properties with fiber alignment by guiding the motion of the bacteria either physically[33] or by setting the growth conditions.[5] After approximately 1 h growth, a two-dimensional network of individually distinguishable cellulose fibers is formed, as illustrated in Figure 3a. The corresponding intensity profile, showing distinct peaks emerging above an insignificant background, confirms

the absence of cellulose fibers outside the focal plane. After 1 day of growth, an increased amount of intersecting fibers in three dimensions can be seen, supported by a minor baseline signal in the profile of Figure 3b. However, individual fibers can still be distinguished. After 2 days, a dense cellulose matrix can be observed, manifested by a significant baseline signal in the profile (Figure 3c), and individual fibers are less distinguishable. Finally, the increase in network fiber density with growth time is further confirmed by Figure 3d, representing a 7 day sample. Quantified as the integrated intensity relative to an image area having all pixels set to the maximum SHG-signal value, which corresponds to an image area completely covered by cellulose fibers, the network densities in the probed sections are 8% (1 h), 9% (1 day), 11% (2 days), and 15% (7 days). While single bacterial cellulose fibers previously have been monitored by darkfield microscopy,[34] noninvasive studies of the end-product morphology have become feasible by the introduction of SHG microscopy.[21] The technique enables resolution of individual cellulose fibers with diameters estimated to ~200 nm (cf. Figure 3A), which corresponds well to what has been determined from replicas of single fibers by electron microscopy (~46 fibrils each 5.8 nm: fibril assembly, fiber 267 nm).[34]

A full radial scan over the wall of a tubular scaffold colocalized with the bacteria is shown in the montage of SHG and CARS microscopy images in Figure 4, where the larger scale allows an observation of supra-structures in the scaffold. The dense network contains cellulose-free regions, cavities (middle arrows in Figure 4), where the simultaneously collected CARS images show higher densities of bacteria compared to the tissue in general. The observation of material cavities is in accordance with previous reports,[35] and the higher density of bacteria indicates that they may host favorable microenvironmental conditions, facilitating the survival of bacteria. The largest amounts of bacteria are found in the peripheral regions of the tube (outer arrows in Figure 4) where emerging cellulose matrices with clearly distinguishable individual fibers can be seen. This indicates these regions as primary sites of growth of the cellulose construct, which can be explained by the higher access to oxygen and nutrients. A three-dimensional view of a cellulose network after tubular growth is shown in Figure 5 and reveals supra-structures in the form of 5–8 μm thick layers of alternating high and low SHG-signal generating cellulose networks, which is supported by previous electron microscopy studies.[5] Different growth conditions determine the degree of molecular order and SHG-efficacy of the cellulose fibers,[14] which indicates local variations in the microenvironment or production rate. Further investigations are needed to explain this phenomenon.

These data illustrate that the combination of nonlinear techniques permits label-free visualization of the biosynthesis process of cellulose in three dimensions, not only as an emerging network of cellulose fibers but also as a dense cellulose matrix containing supra-structures, with the potential to reveal previously unknown mechanisms of bacterial cellulose growth. Moreover, hierarchical structures characteristic for native tissues can be naturally formed in cellulose scaffolds under controlled growth conditions, which can be an instrument to design their end-product strength, elasticity, and cell-interaction properties mimicking that of their natural correspondents.

3.2. Visualization of Cell Integration in Bacterial Cellulose Implants. The interaction of adipose tissue with cellulose scaffolds of different morphology is depicted in Figures 6 (compact cellulose scaffold) and 7 (porous cellulose scaffold) measured in samples taken from subcutaneous implants in rats.
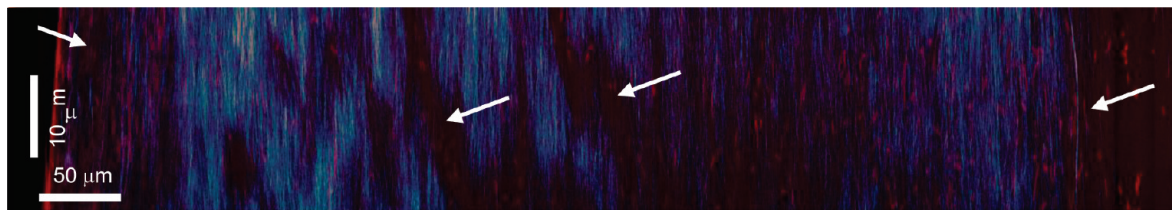
Figure 4. Montage of 25 × 25 μm overlay SHG and CARS microscopy images covering a radial cross section of the wall of a cellulose tube (7 days of growth) from the external (left) to the luminal (right) side. The SHG signal (blue color) shows the radial distribution of cellulose material and the CARS signal (red color) shows the distribution of bacteria in the tube wall. The highest densities of bacteria are found at the peripheral regions of the tube and in internal cavities of the material, positions indicated by arrows. The integration time was 60 s for each subimage.
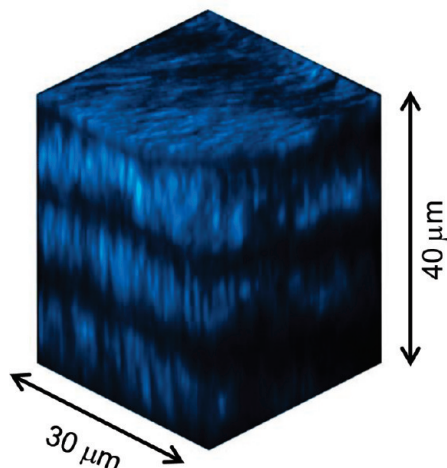

Figure 5. A three-dimensional SHG image (30 × 30 × 40 μm³) of the distribution of cellulose fibers, showing high and low signal generating layers in the transverse plane of a cellulose tube wall. The top surface corresponds to the surface facing the reader in Figure 4. This indicates that a cellulose scaffold grown on an oxygen-fed tubular support is composed of layers with different degree of crystallinity/density, in this case with thicknesses of 5−8 μm.

The lipid-rich native adipocytes are clearly visualized by means of CARS microscopy due to the probing of CH_2 groups and the images are in general agreement with histology on adipose tissue reported in literature. The cellulose fibers in the scaffold and the collagen of the native extracellular matrix (ECM) both appear in the SHG microscopy images, however collagen and cellulose fibers generate SHG signals with different efficacy, thus they can largely be differentiated based on intensity. In addition to generating a stronger SHG signal than cellulose, the imaged collagen fibers also seem arranged in larger, wavy

structures. This is exemplified in the colocalization image of the compact cellulose scaffold (Figure 6), where the collagen can be observed as band-like structures in-between the adipocytes. At the boundary toward the cellulose scaffold, close contact between cells and fibers has been established, but without any significant signs of in-growth into the matrix with the exception of micrometer-sized satellite lipid droplets at the immediate boundary (insert in Figure 6). Thus, this scaffold architecture is favorable as a support for the establishment of an external cell layer, such as endothelial cells forming a biocompatible surface on, for example, the luminal side of artificial blood vessels. However, when the scaffold texture allows for it, micrometer-sized satellite droplets are seeded into the boundary region (inset in Figure 6). This indicates that the degree of cell integration can be controlled by formation of supra-structures in the scaffold.

This is confirmed by the porous scaffold, depicted in Figure 7, showing manifest integration of cells and ECM collagen fibers, despite no surface preparation procedures. In Figure 7a, the cells are partly surrounded by band-like structures of collagen from the ECM (upper left part), bridging over to the more homogeneous cellulose scaffold in the lower right part of the image.

Figure 7b shows a region where an increased integration of cells into the cellulose network and connections with the ECM components can be observed. An integration region is formed in the scaffold hosting ECM collagen bundles, presumably promoting migration of cells from the ECM into the cellulose matrix. Thus, the porous construct lends itself for the functionalization of a larger scaffold volume, for example, by smooth muscle cells or hormone-releasing cells. The interaction between artificial tissue and the natural ECM is important since its components regulate cell differentiation, growth and migration.
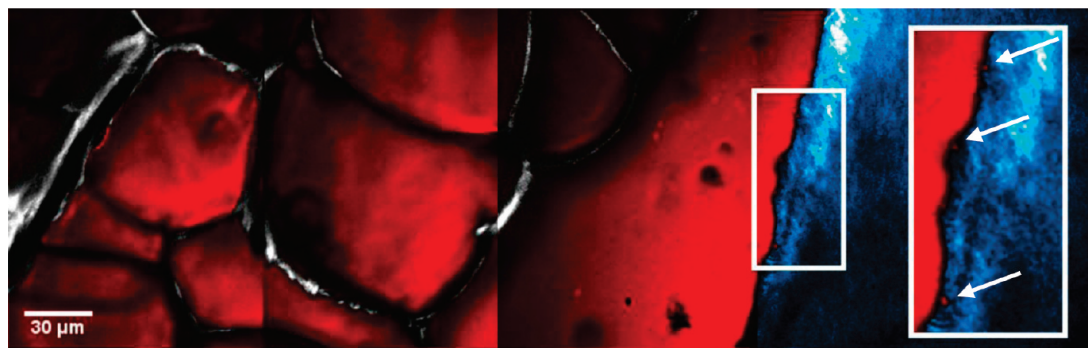
Figure 6. Montage of SHG (blue/gray) and CARS (red) microscopy images (four 150 × 150 μm sized overlay images) of a compact cellulose scaffold and its interaction with the host tissue following implantation in rat. A close interaction with the adipose tissue at the distinct boundary region of the cellulose scaffold can be seen in the zoomed-in inset. Note the micrometer-sized satellite lipid droplets. Connective tissue collagen also generates an SHG signal, though stronger than cellulose. Thus, it can be identified by thresholding and is seen (gray-white) as the band-like structures in between the adipocytes to the left in the montage. No integration into the cellulose scaffold can be observed. Integration time was 20 s per image.
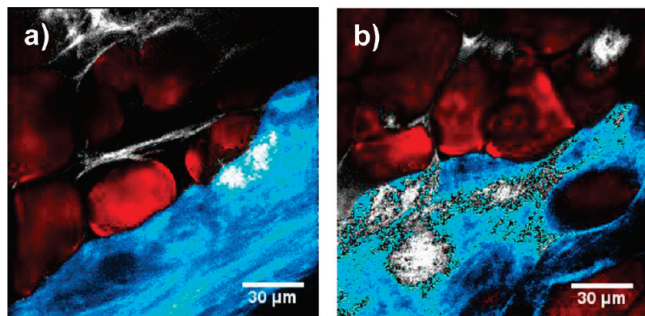
Figure 7. CARS and SHG microscopy overlay images of the manifest cell integration obtained after implantation of porous cellulose scaffolds. (a) Adipocytes (red) surrounded by band-like structures of native collagen (gray-white) from the ECM can be seen in the upper left part, bridging over to the more homogeneous cellulose matrix (blue) in the lower right region of the image. The integration of ECM components from adipose tissue is interesting since it is a source of cells which can be differentiated into several functionalities in the cellulose scaffold. (b) Region showing cells more integrated into the cellulose network and with connections between cellulose and native ECM components. Image size is 150 × 150 μm and the integration time is 20 s.

Figures 6 and 7 show that SHG microscopy offers the attractive ability to visualize this kind of interaction. A further step could be to investigate the integration of ECM-produced elastin with the purpose to improve the elastic properties of the cellulose network, desirable for its function as, for example, artificial vascular tissue. A systematic study where the character of the host tissue in the contact region is standardized is required to conclude this, but this study already indicates that not only the degree of cell integration can be determined by the porosity of the cellulose graft, but also the establishment of native ECM components. This is a particularly important aspect for adipose tissue since, in contrast to bone marrow-derived stem cells; it is a highly accessible and abundant source of multipotent cells which can be differentiated into several lineages beyond adipocytes, such as osteoblasts, hepatocytes, and smooth and cardiac muscle cells, as well as endothelial, hematopoietic, and neuronal cells.[36] By the spontaneous integration of these cells into the cellulose scaffold without any proliferation agents, a wide range of functional properties can be achieved in a convenient way, with the potential of producing replacement tissues with a wide range of functional properties.

4. Conclusion

The properties of nonlinear microscopy techniques allow new, valuable insights to be obtained from investigations of many materials developed in tissue engineering, which in this paper is demonstrated for studies of bacterial cellulose. The initial biosynthesis of nanofibrils and the structure of complete cellulose scaffolds were monitored by means of multimodal nonlinear microscopy, that is, combined second harmonic generation and coherent anti-Stokes Raman scattering microscopy. This allowed visualization of details on a single-fiber level as well as of scaffold supra-structures.

Supra-structures can be implemented in the scaffold architecture by control of cellulose growth conditions and provide the ability to influence scaffold-cell integration, which can be readily monitored by nonlinear microscopy. Measurements on explanted cellulose scaffolds clearly demonstrates this and provided information on the cell interaction properties of compact and porous constructs, illustrating that it is strongly influenced by the scaffold supra-structure. Adipocytes were

arranged in a continuous layer on the compact matrix while the porous construct exhibited manifest integration of both ECM components and cells. This is a significant observation, in particular, for adipose tissue, a convenient source of multipotent cells that can be differentiated into several lineages. It opens up for a wide range of desirable functionalities of the cellulose tissue scaffold, making it a highly attractive and promising material within tissue engineering.

Supporting Information Available. (a) Fluorescence image of a network of bacterial cellulose fibers stained with Congo Red, image size 30 × 30 μm, integration time 20 s. (b) Second harmonic generation image measured in the same field-of-view as the fluorescence image, SHG image integration time 180 s. Only weak signals appear from the cellulose structures, proving that the structure has been disrupted by the staining and illustrating the need for noninvasive, label-free microscopy techniques for the visualization of the fragile cellulose fibers. This material is available free of charge via the Internet at http://pubs.acs.org.

References and Notes

(1) Gilbert, T. W.; Sellaro, T. L.; Badylak, S. F. *Biomaterials* **2006**, *27* (19), 3675–3683.
(2) Buttafoco, L.; Kolkman, N. G.; Engbers-Buijtenhuijs, P.; Poot, A. A.; Dijkstra, P. J.; Vermes, I.; Feijen, J. *Biomaterials* **2006**, *27* (5), 724–734.
(3) Barnes, C. P.; Sell, S. A.; Boland, E. D.; Simpson, D. G.; Bowlin, G. L. *Adv. Drug Delivery Rev.* **2007**, *59* (14), 1413–1433.
(4) Czaja, W. K.; Young, D. J.; Kawecki, M.; Brown, R. M. *Biomacromolecules* **2007**, *8* (1), 1–12.
(5) Bodin, A.; Bäckdahl, H.; Fink, H.; Gustafsson, L.; Risberg, B.; Gatenholm, P. *Biotechnol. Bioeng.* **2007**, *97* (2), 425–434.
(6) Chow, D.; Nunalee, M. L.; Lim, D. W.; Simnick, A. J.; Chilkoti, A. *Mater. Sci. Eng. R* **2008**, *62*, 125–155.
(7) Thomas, V.; Dean, D. R.; Jose, M. V.; Mathew, B.; Chowdhury, S.; Vohra, Y. K. *Biomacromolecules* **2007**, *8* (2), 631–637.
(8) Yan, Z. Y.; Chen, S. Y.; Wang, H. P.; Wang, B.; Wang, C. S.; Jiang, J. M. *Carbohydr. Res.* **2008**, *343* (1), 73–80.
(9) Brown, E. E.; Laborie, M. P. G. *Biomacromolecules* **2007**, *8* (10), 3074–3081.
(10) Luo, H. L.; Xiong, G. Y.; Huang, Y.; He, F.; Wang, W.; Wan, Y. Z. *Mater. Chem. Phys.* **2008**, *110* (2−3), 193–196.
(11) Heydarkhan-Hagvall, S.; Schenke-Layland, K.; Dhanasopon, A. P.; Rofail, F.; Smith, H.; Wu, B. M.; Shemin, R.; Beygui, R. E.; MacLellan, W. R. *Biomaterials* **2008**, *29* (19), 2907–2914.
(12) Minuth, W. W. Strehl, R. K. S. *Tissue Engineering*; Wiley-VCH: Weinheim, 2005.
(13) Abeysekera, R. M.; Robards, A. W.; Hodgson, A. B.; Goodall, D. M. *Int. J. Biol. Macromol.* **1993**, *15* (5), 313–315.
(14) Czaja, W.; Romanovicz, D.; Brown, R. M. *Cellulose* **2004**, *11*, 403–411.
(15) Shao, Z. F.; Mou, J.; Czajkowsky, D. M.; Yang, J.; Yuan, J. Y. *Adv. Phys.* **1996**, *45* (1), 1–86.
(16) Pawley, J. B. *Handbook of Biological Confocal Microscopy*, 3rd ed.; Springer: New York, 2006.
(17) Colvin, J. R.; Witter, D. E. *Protoplasma* **1983**, *116* (1), 24–40.
(18) Campagnola, P. J.; Loew, L. M. *Nat. Biotechnol.* **2003**, *21* (11), 1356–1360.
(19) Williams, R. M.; Zipfel, W. R.; Webb, W. W. *Biophys. J.* **2005**, *88*, 1377–1386.
(20) Plotnikov, S. V.; Millard, A. C.; Campagnola, P. J.; Mohler, W. A. *Biophys. J.* **2006**, *90*, 693–703.
(21) Brown, R. M.; Millard, A. C.; Campagnola, P. J. *Opt. Lett.* **2003**, *28* (22), 2207–2209.

(22) Rice, W. L.; Firdous, S.; Gupta, S.; Hunter, M.; Foo, C. W. P.; Wang, Y.; Kim, H. J.; Kaplan, D. L.; Georgakoudi, I. *Biomaterials* **2008**, *29* (13), 2015–2024.

(23) Cheng, J.-X.; Xie, X. S. *J. Phys. Chem. B* **2004**, *108*, 827–840.

(24) Cheng, J.-X. *Appl. Spectrosc.* **2007**, *91*, 197–208.

(25) Wang, H.-W.; Le, T. T.; Cheng, J.-X. *Opt. Commun.* **2008**, *281*, 1813–1822.

(26) Schenke-Layland, K.; Riemann, I.; Stock, U. A.; Köing, K. *J. Biomed. Opt.* **2005**, *10* (2), 024017.

(27) Sun, Y.; Tan, H.-Y.; Lin, S.-J.; Lee, H.-S.; Lin, T.-Y.; Jee, S.-H.; Young, T.-H.; Lo, W.; Chen, W.-L.; Dong, C.-Y. *Microsc. Res. Tech.* **2008**, *71*, 140–145.

(28) Georgakoudi, I.; Rice, W. L.; Hronik-Tupaj, M.; Kaplan, D. L. *Tissue Eng.* **2008**, *14* (4), 321–340.

(29) Matsuoka, M.; Tsuchida, T.; Matsushita, K.; Yoshinaga, F. *Biosci., Biotechnol., Biochem.* **1996**, *60* (4), 575–579.

(30) White, D. G.; Brown, R. M., Jr. Prospects for the Commercialization of the Biosynthesis of Microbial Cellulose. *Cellulose and Wood*; Wiley: New York, 1989.

(31) Bäckdahl, H.; Esguerra, M.; Delbro, D.; Risberg, B.; Gatenholm, P. *J. Tissue Eng. Regen. Med.* **2008**, *2* (6), 320–330.

(32) Helenius, G.; Backdahl, H.; Bodin, A.; Nannmark, U.; Gatenholm, P.; Risberg, B. *J. Biomed. Mater. Res., Part A* **2006**, *76A* (2), 431–438.

(33) Kondo, T.; Togawa, E., Jr., R. M. B. *Biomacromolecules* **2001**, *2* (4), 1324–1330.

(34) Brown, R. M.; Willison, J. H. M.; Richardson, C. L. *Proc. Natl. Acad. Sci. U.S.A.* **1976**, *73* (12), 4565–4569.

(35) Thompson, N. S.; Carlson, J. A.; Kaustinen, H. M.; Uhlin, K. I. *Int. J. Biol. Macromol.* **1988**, *10* (2), 126–127.

(36) Schaffler, A.; Buchler, C. *Stem Cells* **2007**, *25* (4), 818–827.